A sub-millitesla Ge spin qubit

Daniel Jirovec[1], Andrea Hofmann[1], Andrea Ballabio[2], Philipp M. Mutter[3], Giulio Tavani[2], Marc Botifoll[4], Alessandro Crippa[1], Josip Kukucka[1], Oliver Sagi[1], Frederico Martins[1], Jaime Saez-Mollejo[1], Ivan Prieto[1], Maksim Borovkov[1], Jordi Arbiol[4,5], Daniel Chrastina[2], Giovanni Isella[2], Georgios Katsaros[1]

[1]Institute of Science and Technology Austria, Am Campus 1, 3400 Klosterneuburg, Austria
[2]L-NESS, Physics Department, Politecnico di Milano, via Anzani 42, 22100, Como, Italy
[3]Department of Physics, University of Konstanz, D-78457 Konstanz, Germany
[4]Catalan Institute of Nanoscience and Nanotechnology (ICN2), CSIC and BIST, Campus UAB, Bellaterra, Barcelona, Catalonia, Spain
[5]ICREA, Passeig de Lluís Companys 23, 08010 Barcelona, Catalonia, Spain

October 19, 2020

Abstract

Spin qubits are considered to be among the most promising candidates for building a quantum processor[1]. Just recently, a four qubit device, operating at 1 tesla, was demonstrated[2]. The, so far hindered, operation at very low fields would further improve their prospects in terms of scalability and high fidelity fast readout, as it will facilitate their integration with superconducting circuits such as Josephson parametric amplifiers, superconducting resonators and superconducting quantum interference devices[3;4;5;6]. Here we demonstrate a hole spin qubit operating already at 500 µT, within the range of magnetic fields currently used for on-chip biasing of superconducting circuits[7]. This is achieved by exploiting the large out-of-plane Ge heavy hole g-factors and by encoding the qubit into the singlet-triplet states of a double quantum dot[8;9]. We observe electrically controlled X and Z-rotations with tunable frequencies exceeding 100 MHz and dephasing times of 1 µs which we extend beyond 10 µs with echo techniques. Strikingly, the X-rotation frequency can be increased without shortening the dephasing time of the qubit. The reported results, together with the already demonstrated proximity induced superconductivity[10;11], show that the planar Ge platform can merge semiconductor qubits with superconducting technologies.

Holes in Ge have emerged as one of the most promising spin qubit candidates[13] because of their particularly strong spin orbit coupling (SOC)[14], which leads to record manipulation speeds[15;16], and low dephasing rates[16]. In addition, the SOC together with the low effective mass[17] relax fabrication constrains, and larger quantum dots can be operated as qubits without the need for microstrips and micromagnets. In only three years a single Loss-DiVincenzo qubit[18], 2-qubit and most recently even 4-qubit devices have been demon-

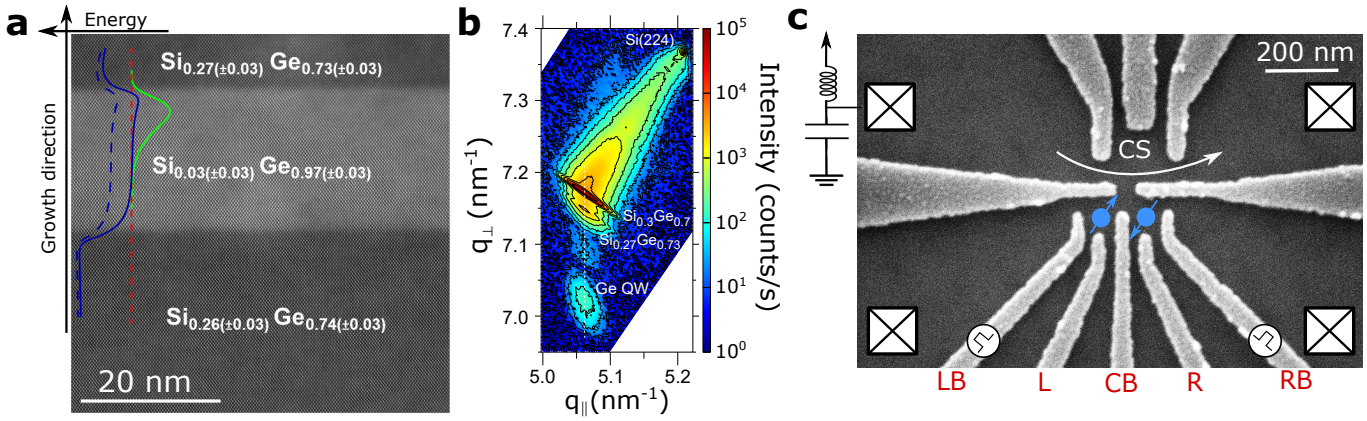

Figure 1: Heterostructure and gate layout. a) Atomic resolution HAADF-STEM image of the heterostructure showing sharp interfaces at the top and bottom of the quantum well. The stoichiometry of the three layers has been determined by electron energy-loss spectroscopy (see Supplementary). The heavy hole (solid blue line) and light hole (dashed blue line) band energies as a function of growth direction are superimposed to the picture. The red dashed line represents the fermi energy. Heavy holes are accumulated at the upper QW interface as shown by the bright green line representing the heavy hole wave function density (simulations were performed in NextNano). b) X-ray diffraction (XRD) reciprocal space map (RSM) around the Si (224) Bragg peak, present at the top right of the map. The graded buffer is visible as a diffuse intensity between the Si peak and the $Si_{0.3}Ge_{0.7}$ peak, while the $Si_{0.3}Ge_{0.7}$ peak itself corresponds to the 2 µm constant composition layer at the top of the buffer. The Ge QW peak is aligned vertically below the $Si_{0.3}Ge_{0.7}$ VS, as shown by the dotted line, indicating that it has the same in-plane lattice parameter, i.e. that the Ge QW is lattice-matched to the VS. The intensity just below the VS peak indicates that the true Ge content in the barriers on either side of the Ge QW is about 73%. c) Scanning electron microscope (SEM) image of the gate layout used for this experiment. We note that without the application of any negative accumulation voltage we measure a charge carrier density of $9.7 \times 10^{11}\mathrm{cm}^{-2}$. Secondary ion mass spectroscopy (SIMS) rules out boron doping as a source for this carrier density. We thus attribute the measured hole density to the fixed negative charges in the deposited oxide which can act as an accumulation gate[12].

strated[2;19;20]. Here we show that by implementing Ge hole spin qubits in a double quantum dot (DQD) device they have the further appealing feature that operation below the critical field of aluminium becomes possible.

In order to realize such a qubit a strained Ge quantum well (QW) structure, with a hole mobility of $1.0 \times 10^5\mathrm{cm}^2/\mathrm{Vs}$ at a density of $9.7 \times 10^{11}\mathrm{cm}^{-2}$, was grown by low-energy plasma-enhanced chemical vapor deposition (LEPECVD). Starting from a Si wafer a 10 µm thick strain-relaxed $Si_{0.3}Ge_{0.7}$ virtual substrate (VS) is obtained by linearly increasing the Ge content during the epitaxial growth. The $\approx$ 20 nm thick strained Ge QW is then deposited and capped by 20 nm of $Si_{0.3}Ge_{0.7}$. In Fig. 1a we show the aberration corrected (AC) high-angle annular dark-field scanning transmission electron microscopy (HAADF-STEM) image of our heterostructure. The HAADF Z-contrast clearly draws the sharp interfaces between the QW and the top and bottom barriers. In addition, x-ray diffraction (XRD) measurements highlight the lattice matching between the virtual substrate and the QW (Fig. 1b). Holes confined in such a QW are of heavy-hole (HH) type because compressive strain and confinement move light-holes (LHs) to higher hole energies[21]. The related Kramers doublet of the spin $S_z = \pm 3/2$ states therefore resembles an effective spin-1/2 system, $|\uparrow\rangle$ and $|\downarrow\rangle$.

In a singlet-triplet qubit the logical quantum states are defined in a 2-spin 1/2 system with total spin along the quantization axis $S_Z = 0$[8;9]. This is achieved by confining one spin in each of two tunnel coupled quantum dots, formed by depletion gates (Fig. 1c). We tune our device into the single hole transport regime, as shown by the stability diagram in Fig. 2 where the sensor dot reflected phase signal (Φ_{refl}) is displayed as a function of the voltage on L and R (see Methods and Supplementary). Each Coulomb blocked region corresponds to a fixed hole occupancy, and is labeled by (N_L, N_R), with N_L (N_R) being the equivalent number of holes in the left (right) quantum dot; interdot and dot-lead charge transitions appear as steep changes in the sensor sig-

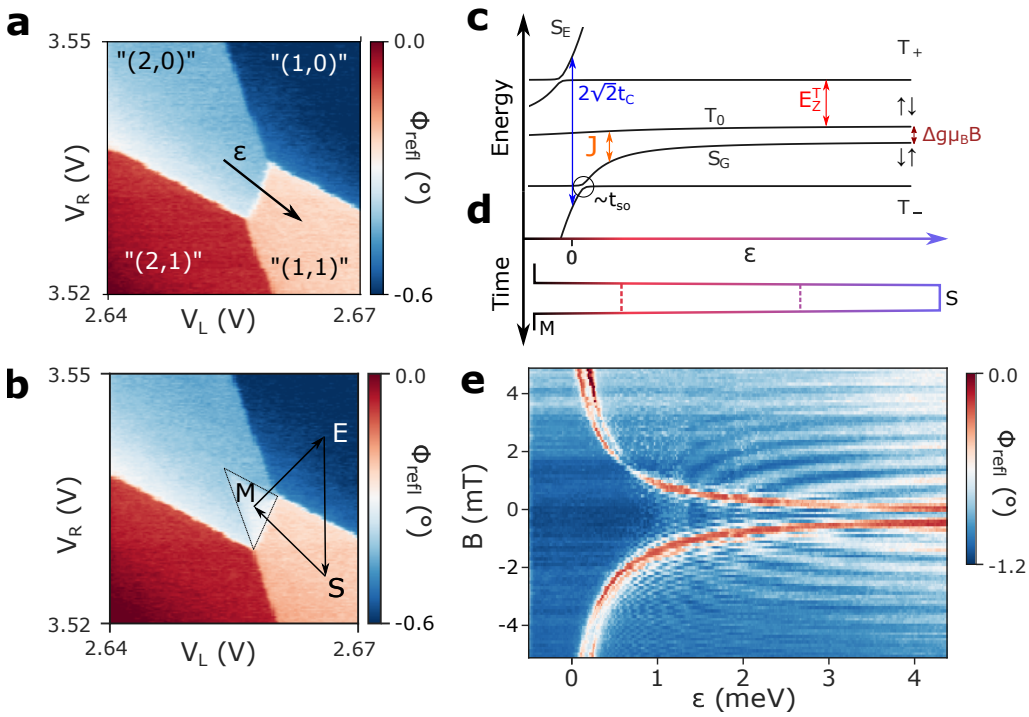

Figure 2: Pauli spin blockade and dispersion relation. a) Stability diagram of the region of interest. The effective number of holes in each Coulomb blocked island is defined as "(N_L,N_R)". The quotes symbolize an equivalent hole number. The real hole number is $N_L = 3$ or 4 depending on the blockade region, and $N_R = 2n$ or $2n+1$ where n is an integer (see Supplementary). We will omit the quotes in the following. The diagonal arrow highlights the detuning (ϵ) axis. b) Stability diagram acquired while pulsing in a clockwise manner following the arrows. The system is emptied (E) in (1,0) and pulsed to (1,1) (separation point S) where either a singlet or a triplet will be loaded. Upon pulsing to the measurement point (M) in (2,0) the triplet states are blocked leading to the marked triangular blockade region. c) Energy dipsersion relation as a function of ϵ at finite magnetic field. $\epsilon = 0$ is defined at the $(2,0) \leftrightarrow (1,1)$ resonance. At high ϵ the Hamiltonian has four eigenstates: two polarized triplets $|T_-\rangle = |\downarrow\downarrow\rangle$, $|T_+\rangle = |\uparrow\uparrow\rangle$ and two anti-parallel spin states $|\uparrow\downarrow\rangle$, $|\downarrow\uparrow\rangle$. The triplet Zeeman energy $E_Z^T = \pm\Sigma g\mu_B B/2$ (red) lifts the degeneracy of the triplets. The singlet energy $E_S = \frac{\epsilon}{2} - \sqrt{\frac{\epsilon^2}{4} + 2t_C^2}$, where t_C is the tunnel coupling between the dots, anti-crosses with the polarized triplet states due to spin-orbit interaction parametrized by t_{SO}. The singlet $S_G := S$ and triplet T_0 are split in energy by the exchange interaction $J = |E_S - E_{T_0}|$ which decreases with increasing ϵ. d) Pulse sequence adopted to acquire e). Starting from (2,0) the system is pulsed to (1,1) at varying ϵ, left evolving for 100 ns and then pulsed back to measure in M. e) Spin funnel confirming c) and the validity of assuming an effective hole number of (2,0) and (1,1). When $J(\epsilon) = E_Z^T$ the triplet signal (red) increases as a result of $S - T_-$ intermixing. Around the funnel $S - T_-$ oscillations can be observed while at higher detuning $S - T_0$ oscillations become more prominent.

nal. By pulsing in a clockwise manner along the E-S-M vertices (Fig. 2b) we observe a triangular region leaking inside the upper-left Coulomb blocked region. Such a feature identifies the metastable region where Pauli spin blockade (PSB) occurs: once initialized in E ('empty'), the pulse to S loads a charge and the spins are separated forming either a spin singlet or a triplet. At the measurement point M within the marked triangle, the spin singlet state leads to tunnel events, while the triplet states remain blocked, which allows spin-to-charge conversion. We repeat the experiment with a counter-clockwise ordering (E-M-S) and no metastable region is observed, as expected (Fig. 2a was acquired while pulsing in the counter-clockwise ordering). We thus consider the inter-dot line across the detuning (ϵ) axis of Fig. 2a equivalent to the $(2,0) \leftrightarrow (1,1)$ effective charge transitions. The system is tuned along the detuning axis from (2,0) to (1,1) by appropriately pulsing on LB and RB (see Sup-

plementary). The DQD spectrum for a finite B field is reported in Fig. 2c (the triplet states T(2,0) lie high up in energy and are not shown; the model Hamiltonian is derived in supplementary section 1). We set $\epsilon = 0$ at the $(2,0) \leftrightarrow (1,1)$ crossing. Starting from (2,0) increasing ϵ mixes (2,0) and (1,1) into two molecular singlets; the ground state $S_G := S$ and the excited state S_E, neglected in the following, which are split at resonance by the tunnel coupling $2\sqrt{2}t_C$. The triplet states are almost unaffected by changes in ϵ. We define the exchange energy J as the energy difference between $S = \frac{1}{\sqrt{2}}(|\uparrow\downarrow\rangle - |\downarrow\uparrow\rangle)$ and the unpolarized triplet $T_0 = \frac{1}{\sqrt{2}}(|\uparrow\downarrow\rangle + |\downarrow\uparrow\rangle)$. At large positive detuning J drops due to the decrease of the wavefunction overlap for the two separated holes; importantly, different g-factors for the left (g_L) and the right dot (g_R) result in four (1,1) states: two polarized triplets $|T_-\rangle = |\downarrow\downarrow\rangle$, $|T_+\rangle = |\uparrow\uparrow\rangle$ and two anti-parallel spin states $|\uparrow\downarrow\rangle$, $|\downarrow\uparrow\rangle$ split by $\Delta E_Z = \Delta g \mu_B B$, where $\Delta g = |g_L - g_R|$, μ_B is the Bohr magneton and B is the magnetic field applied in the out-of-plane direction. However, as noticed later, even at large positive ϵ a residual J persists, which leads to the total energy splitting between $|\uparrow\downarrow\rangle$ and $|\downarrow\uparrow\rangle$ being $E_{tot} = \sqrt{J(\epsilon)^2 + (\Delta g \mu_B B)^2}$. By applying a pulse with varying ϵ (Fig. 2d) and stepping the magnetic field we obtain the plot in Fig. 2e drawing a funnel. The experiment maps out the degeneracy between $J(\epsilon)$ and $E_Z^T = \pm\frac{\Sigma g \mu_B B}{2}$, where E_Z^T is the Zeeman energy of the polarized triplets and $\Sigma g = g_L + g_R$. The doubling of the degeneracy point can be attributed to fast spin-orbit induced $S - T_-$ oscillations[22]. At larger detuning $S - T_0$ oscillations become visible.

The effective Hamiltonian of the qubit subsystem is:

$$H = \begin{pmatrix} -J(\epsilon) & \frac{\Delta g \mu_B B}{2} \\ \frac{\Delta g \mu_B B}{2} & 0 \end{pmatrix} \tag{1}$$

in the $\{|S\rangle, |T_0\rangle\}$ basis, with $J(\epsilon)$ being the detuning-dependent exchange energy, common to all $S - T_0$ qubits. Here the $S - T_0$ coupling is controlled both directly via the magnetic field and by electric fields affecting the g-factors[23]. Pulsing on ϵ influences J and the ratio between J and $\Delta g \mu_B B$ determines the rotation axis tilted by an angle $\theta = \arctan\left(\frac{\Delta g \mu_B B}{J(\epsilon)}\right)$ from the Z-axis. For large detuning $\theta \to 90°$ corresponding to X-rotations while for small detuning $\theta \to 0°$ enabling Z-rotations.

A demonstration of coherent X-rotations at a center barrier voltage $V_{\mathrm{CB}} = 910\,\mathrm{mV}$ is depicted in Fig. 3c with the pulse sequence shown in Fig. 3b. The system is first initialized in (2,0) in a singlet, then pulsed quickly deep into (1,1) where the holes are separated. Here the state evolves in a plane tilted by θ (Fig. 3a, Fig. 3d). After a separation time τ_S the system is brought quickly to the measurement point in (2,0) where PSB enables the distinction of triplet and singlet. Varying τ_S produces sinusoidal oscillations with frequency $f = \frac{1}{h}\sqrt{J^2 + (\Delta g \mu_B B)^2}$ (Fig. 3e), where h is the Planck constant. We extract $\Delta g = 2.04 \pm 0.04$ and $J(\epsilon = 4.5\,\mathrm{meV}) \approx 21\,\mathrm{MHz}$. We approach frequencies of 100 MHz at fields as low as 3 mT. Fig. 3f shows the extracted singlet probability $\mathrm{P_S}$ at different magnetic fields. The black solid line is a fit to $\mathrm{P_S} = A\cos(2\pi f \tau_s + \phi)\exp\left(-(t/T_2^*)^2\right) + C$, where T_2^* is the inhomogeneous dephasing time. $\mathrm{P_S}$ only oscillates between 0.5 and 1 as a direct consequence of $J(\epsilon = 4.5\,\mathrm{meV}) \neq 0$ and the tilted rotation axis. One would expect an increase in the oscillation amplitude with higher magnetic field. However, at large ΔE_Z the T_0 state quickly decays to the singlet during read-out, reducing the visibility as is clearly shown by the curve at 2 mT in Fig. 3f. This can be circumvented by different read-out schemes such as latching[24] or shelving[25] but this is out of the scope of the present work, which focuses on the low magnetic field behavior.

We, furthermore, observe a dependence of Δg on the voltage on CB (Fig. 3g) confirming electrical control over the g-factors. As the voltage is decreased by 50 mV, Δg varies from ≈ 1.5 to more than 2.2 which conversely increases the frequency of X-rotations. Concurrently we measure a similar trend in T_2^* reported at $B = 1\,\mathrm{mT}$ in Fig. 3h; as the center barrier is lowered the coherence of the qubit is enhanced. The origin and consequences of this observation are discussed later.

Next, we demonstrate full access to the Bloch sphere achieved by Z-rotations leveraging the exchange interaction. We change the pulse sequence (Fig. 4b) such that after initialization in a singlet the system is pulsed to large detuning but is maintained in this position only for $t = t_{\pi/2}$ corresponding to a $\pi_x/2$ rotation , bringing the system close to $i\,|\uparrow\downarrow\rangle$. Now we let the state evolve for a

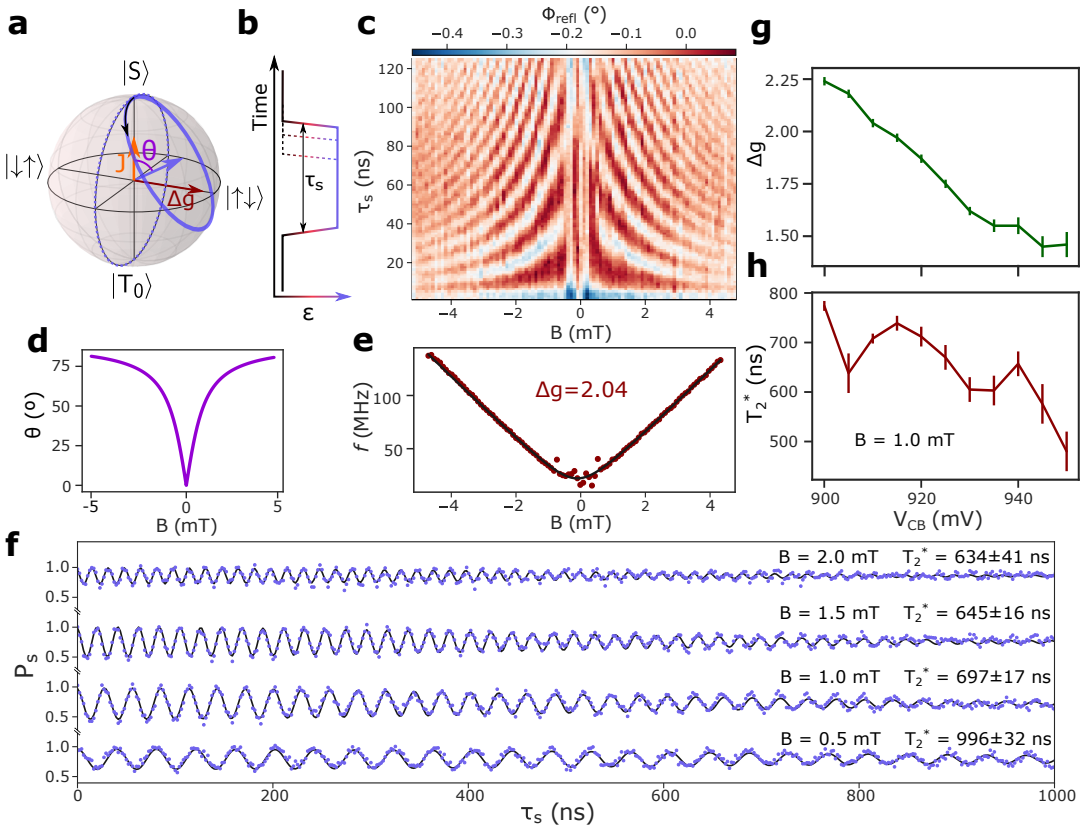

Figure 3: X-rotations. a) State evolution on the Bloch sphere. X-rotations are controlled by Δg and the applied magnetic field. The ideal rotation axis is depicted as a dark red arrow. The dashed purple trajectory corresponds to a perfect X-rotation while the effective rotation axis is tilted by an angle θ from the z-axis due to a finite residual J (orange arrow pointing along the Z-axis) resulting in the state evolution depicted by the solid purple curve. b) Pulse sequence used for performing the X-rotations. After initialization in a singlet the separation time τ_S is varied while the amplitude is $\epsilon = 4.5\,\mathrm{meV}$. The system is then diabatically pulsed back to the measurement point. c) X-oscillations as a function of magnetic field and separation time at $V_{CB} = 910\,\mathrm{mV}$. The average of each column has been substracted to account for variations in the reflectometry signal caused by magnetic field. A low (high) signal corresponds to a higher singlet (triplet) probability. Each point is integrated for 100 ms under continuous pulsing (see Supplementary). d) $\theta = \arctan\frac{\Delta g \mu_B B}{J(2.8meV)}$ versus magnetic field. The effective oscillation axis is magnetic field dependent and approaches 80° for B = 5 mT. e) Frequency of X-oscillations as a function of magnetic field. The black line is a fit to $f = \frac{1}{h}\sqrt{J^2 + (\Delta g \mu_B B)^2}$ where we extract a g-factor difference $\Delta g = 2.04 \pm 0.04$ and a residual exchange interaction $J(\epsilon = 4.5\,\mathrm{meV}) = 20 \pm 1\mathrm{MHz}$. We reach frequencies of 100 MHz at fields as low as 3 mT. f) Singlet probability P_S as a function of τ_S at different B-fields for $V_{CB} = 910\,\mathrm{mV}$ extracted through averaged single shot measurements (see Supplementary). The solid lines are a fit to $P_S = A\cos(2\pi f \tau_S + \phi)\exp(-(t/T_2^*)^2) + C$. Because of the tilted angle P_S oscillates only between 0.5 and 1. Moreover, we observe a further decrease in visibility at higher magnetic fields due to decay mechanisms during the read-out process. The extracted T_2^* shows a magnetic field dependence explainable by equation (2). g) g-factor difference as a function of the center barrier voltage V_{CB}. By opening the center barrier the g-factor difference increases from 1.50 to 2.25. h) T_2^* vs V_{CB}. A near doubling in coherence time with lower center barrier voltage is consequence of an increased tunnel coupling (Fig. 4h) as explained in the main text.

time τ_S at a smaller detuning, increasing J and changing the rotation angle θ (Fig. 4d), before applying another $\pi_x/2$ rotation at high detuning and pulsing back to read-out. The state evolution on the Bloch sphere in Fig. 4a shows that full access to the qubit space can be obtained by a combination of appropriately timed pulses. The resulting oscillation pattern is depicted in Fig. 4c. From the inferred frequency we find the dependence of J on

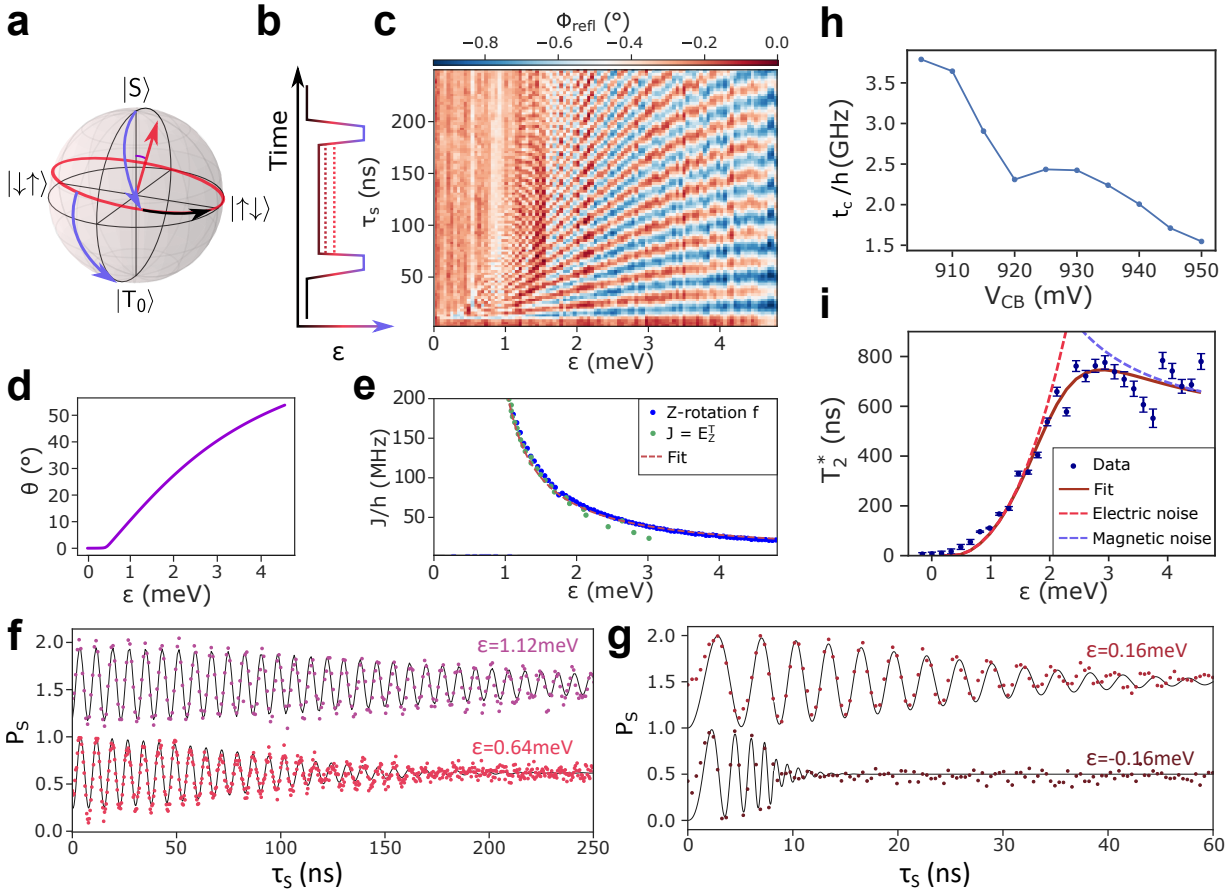

Figure 4: Z-rotations at $B = 1\,\mathrm{mT}$ and $V_{\mathrm{CB}} = 910\,\mathrm{mV}$. a) State evolution on the Bloch sphere. The purple arrows represent $\frac{\pi_x}{2}$-pulses applied at maximum detuning while the red trajectory corresponds to the free evolution at smaller ϵ. b) Pulse sequence used to probe Z-rotations. A $\frac{\pi_x}{2}$-pulse prepares the state close to the equator of the Bloch sphere, where it subsequently precesses under the influence of J. Another $\frac{\pi_x}{2}$-pulse maps the final state on the qubit basis for read-out. c) Z-rotations as a function of τ_S and ϵ. The acquisition method is the same as in Fig. 3c). d) Rotation angle θ as a function of ϵ for B $= 1\,\mathrm{mT}$ and J extracted from c). e) $J/h = \sqrt{f(\epsilon)^2 - (\Delta g \mu_B B/h)^2}$ as a function of ϵ as extracted from the oscillation frequency in c) (blue markers). Green dots correspond to the spin funnel (Fig. 2e) condition $J(\epsilon) = E_Z^T$ with $\Sigma g = 11$ and the red dashed line is the best fit to $J(\epsilon) = \left|\frac{\epsilon}{2} - \sqrt{\frac{\epsilon^2}{4} + 2t_C^2}\right|$. f,g) $\mathrm{P_S}$ as a function of τ_S for different ϵ and offset of $+1$ for clarity. The pulse sequence adopted here increases the amplitude of oscillations as compared to Fig. 3f enabling full access to the Bloch sphere. At very low ϵ we observe the signal to chirp towards the correct frequency as a direct consequence of a finite pulse rise time. As a result, the coherence time is overestimated. h) tunnel coupling t_C/h as a function of V_{CB} demonstrating good control over the tunnel barrier between the two quantum dots. i) T_2^* as a function of ϵ. The dark red solid line is a fit to equation (2). We find $\delta\epsilon_{rms} = 7.59 \pm 0.49\,\mu\mathrm{eV}$, in line with comparable experiments, and $\delta E_{Zrms} = 1.78 \pm 0.01\,\mathrm{neV}$, smaller by a factor 2 than in a comparable natural Si qubit [26]. The bright red (violet) dashed line represents the individual electric (magnetic) noise contribution. For low detuning clearly charge noise is limiting, while at large detuning magnetic noise becomes dominant.

ϵ and extract $t_C/h = 3.64\,\mathrm{GHz}$ as a free fitting parameter. The extracted values of J are plotted in Fig. 4e with the blue markers obtained from the exchange oscillation frequency. The green dots, on the other hand, correspond to $J(\epsilon) = E_Z^T = \frac{\Sigma g \mu_B B}{2}$ extracted from the funnel experiment (Fig. 2e). We find that the two sets of data points coincide when $\Sigma g = 11.0$. Together with the g-factor difference already reported we obtain the two

out-of-plane g-factors to be 4.5 and 6.5, comparable to previous studies[27] . In Fig. 4f and g we plot P_S as a function of separation time at different values of ϵ. P_S now oscillates between 0 and 1 due to the combination of $\pi/2$-pulses and free evolution time at lower detuning. From the fits (black solid lines) at different detunings we extract T_2^* as a function of ϵ (Fig.4i). For low ϵ the coherence time is shorter than 10 ns, while it increases for larger ϵ and saturates at around 2 meV. This is explained by a simple noise model[26;28] where T_2^* depends on electric noise on J and magnetic noise affecting ΔE_Z:

$$\frac{1}{T_2^*} = \frac{\pi\sqrt{2}}{h}\sqrt{\left(\frac{J(\epsilon)}{E_{tot}}\frac{dJ}{d\epsilon}\delta\epsilon_{rms}\right)^2 + \left(\frac{\Delta E_Z}{E_{tot}}\delta\Delta E_{Zrms}\right)^2}, \tag{2}$$

where $\delta\epsilon_{rms}$ is the rms noise on detuning, $\delta\Delta E_{Zrms}$ is the magnetic noise. We assume $\frac{d\Delta E_Z}{d\epsilon} \approx 0$ as we observe almost no change in Δg with detuning (see Supplementary). From the fit (dark red solid line) we find $\delta\epsilon_{rms} = 7.59 \pm 0.35\,\mu\text{eV}$, in line with comparable experiments[26;28], and $\delta E_{Zrms} = 1.78 \pm 0.10\,\text{neV}$. Although $\delta\Delta E_{Zrms}$ is much smaller than $\delta\epsilon_{rms}$ we find that at large detuning coherence is still limited by magnetic noise because $\frac{dJ}{d\epsilon} \to 0$ (see red and violet dashed lines in Fig. 4i). We attribute the magentic noise to randomly fluctuating hyperfine fields caused by spin-carrying isotopes in natural Ge. Eq. (2) also gives insight into the trends observed in Fig. 3f and h. With B we now affect ΔE_Z and, thereby, its contribution to the total energy. The higher ratio $\Delta E_Z/E_{tot}$ the more the coherence is limited by magnetic noise as confirmed by the drop in T_2^* with magnetic field in Fig. 3f. Similarly one would expect that by increasing Δg, T_2^* should be lower. But, as shown in Fig. 4h, the raising g-factor difference is accompanied by an increase of the tunnel coupling by 2 GHz. Hence, J is larger at lower V_{CB} and $\frac{\Delta E_Z}{E_{tot}}$ is reduced leading to a longer T_2^*. While V_{CB} affects both t_C and Δg, we see that V_{LB} and V_{RB} affect mostly t_C and leave Δg unaltered (see Supplementary). This exceptional tunability enables electrical engineering of the potential landscape to favor fast operations without negatively affecting the coherence times, thus enhancing the quality factor of this qubit. While the longest T_2^* reported here is already comparable to electron singlet-triplet qubits in natural Si, a reduction in the magnetic noise contribution by isotopic purification could further improve qubit coherence and quality[29].

We now focus on extending the coherence of the qubit by applying refocusing pulses similar to those developed in nuclear magnetic resonance (NMR) experiments. We investigate the high ϵ region where charge noise is lowest. Exchange pulses at $\epsilon = 0.64\,\text{meV}$ are adopted as refocusing pulses. We note, however, that to obtain a perfect correcting pulse, it would be necessary to implement a more complex pulse scheme[30]. We choose convenient τ_S values ($\tau_S = (2n + \frac{1}{2})t_{\pi_x}$) such that, if no decoherence has occurred, the system will always be found in the same state after τ_S. The refocusing pulse is then calibrated to apply a π-pulse that brings the state on the same trajectory as before the refocusing pulse (Fig. 5a). The free evolution time after the last refocusing pulse $\tau_{s'}$ is varied in length from $\tau_s - \delta t$ to $\tau_s + \delta t$ (Fig. 5b,c) and we observe the amplitude of the resulting oscillations (Fig. 5e). Also, we increase the number of applied pulses from $n_\pi = 1$ to $n_\pi = 16$, thereby increasing the total free evolution time of the qubit and performing a Carr-Purcell-Meiboom-Gill echo. The decay is fit to a Gaussian decay and we extract a T_2^{Echo} of 1.8 µs for $n_\pi = 1$ and $T_2^{Echo} = 16\,\mu\text{s}$ for $n_\pi = 16$ (Fig. 5d) similar to the T_2^{Echo} for $n_\pi = 16$ reported recently for a Ge Loss Di Vincenzo qubit[2]. Furthermore, we observe a power law dependence of T_2^{Echo} as a function of the number of refocusing pulses and find $T_2^{Echo} \approx n_\pi^\beta$ with $\beta = 0.8$. This number is similar to other reported studies in $S - T_0$ qubits in GaAs[31] suggesting that either the materials or the type of qubit have a similar noise spectral density. Refocusing pulses exploiting the symmetric exchange operation could help increasing T_2^{Echo} further since they are carried out at a charge noise sweet spot[32].

In conclusion we have shown coherent 2-axis control of a hole singlet-triplet qubit in Ge with a coherence time of 1µs at 0.5 mT. In most of the so far reported singlet-triplet qubits, X-oscillations were driven by magnetic field differences generated either by nuclear spins [9;33;34] or by fabricated micromagnets[26]. Here we have taken advantage of an intrinsic property of heavy hole

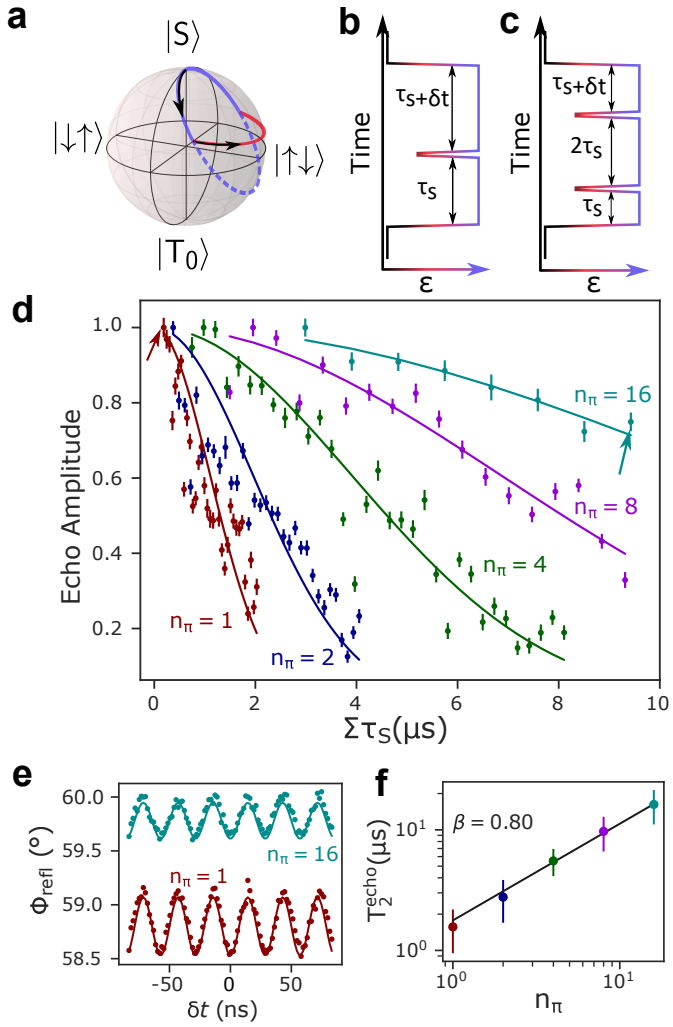

Figure 5: Spin Echo. a) State evolution on the Bloch sphere. The state evolves on the violet trajectory. At appropriate times a short exchange pulse is applied and the state follows the red trajectory followed by another free evolution on the violet trajectory. The free evolution times are chosen as $\tau_s = (2n + 1/2)t_{\pi_x}$ where t_{π_x} is the time needed for a π-rotation along the violet trajectory. b,c) Pulse sequence for one and two refocusing pulses. The last free evolution is $\tau_s' = \tau_s + \delta t$. d) Normalized echo amplitude as a function of total separation time. Solid lines are a fit to $A_E \exp\left(-t/T_2^{Echo}\right)$ with A_E being the normalized echo amplitude. By increasing the number of π-pulses from 1 to 16 the coherence time increases accordingly from $\mathrm{T}_2^{\mathrm{Echo}}(\mathrm{n}_\pi = 1) = 1.8 \pm 0.7\,\mu\mathrm{s}$ to $\mathrm{T}_2^{\mathrm{Echo}}(\mathrm{n}_\pi = 16) = 16.4 \pm 0.4\,\mu\mathrm{s}$. e) Examples of $S - T_0$ oscillations as a function of δt taken for the points highlighted by arrows in d). For $\mathrm{n}_\pi = 1$ $\Sigma\tau_S = 120\,\mathrm{ns}$ while for $\mathrm{n}_\pi = 16$ $\Sigma\tau_S = 10\,\mu\mathrm{s}$. Solid lines are fit to the data with the amplitude and phase as free parameters (an offset of +1 has been added for clarity). f) Power law dependence of $\mathrm{T}_2^{\mathrm{Echo}}$ vs n_π. The exponent β can be used to estimate the noise spectral density which we find comparable to similar qubits in GaAs. [31]

states in Ge, namely their large and electrically tunable g-factors. We have shown electrically driven X-rotation frequencies approaching 150 MHz at fields of 5 mT, which are larger than most of the reported hole spin qubit Rabi frequecies[35;2;19;20]. We observe a T_2^* that exceeds those found in GaAs $S - T_0$ qubits, owing to a lower magnetic

noise contribution, while being comparable to values reported for natural Si. This indicates that, although holes in Ge are to first order insensitive to hyperfine interaction, the spin-carrying isotopes might still limit the coherence of Ge qubits. Most strikingly, by tuning V_{CB} we are able to increase the X-rotation frequency by a factor of 1.5 while nearly doubling the inhomogeneous dephasing time of the qubit. We attribute this observation to electric tunability of the hole g-factors in combination with optimized ratios of electric and magnetic noise contributions.

In the future, latched or shelved read-out could circumvent the decay of T_0 to singlet during read-out opening the exploration of the qubit's behavior at slightly higher magnetic fields where the X-rotation frequencies could surpass the highest electron-dipole spin-resonance Rabi frequencies reported so far[15;16], without suffering from reduced dephasing times. Furthermore, by moving towards symmetric operation or resonant driving the quality of exchange oscillations can be increased since the qubit is operated at an optimal working point[32;36;37;29]. The long coherence times combined with fast and simple operations at extremely low magnetic fields make this qubit an optimal candidate for integration into a large scale quantum processor.

Methods *Quantum well growth:* The strained Ge QW structure was grown by low-energy plasma-enhanced chemical vapor deposition (LEPECVD) and features a $Si_{0.3}Ge_{0.7}$ virtual substrate (VS) grown on a 100 mm Si(001) wafer[38]. The VS is comprised of a graded buffer region approximately 10 μm thick in which the Ge content was increased linearly from pure Si up to the desired final composition of $Si_{0.3}Ge_{0.7}$. The substrate temperature was reduced from 760 to 550°C with increasing Ge content. The buffer was completed with a 2 μm region at a constant composition of $Si_{0.3}Ge_{0.7}$. This part is concluded in about 30 min, with a growth rate of 5-10 nm^{-1} due to the efficient dissociation of the precursor gas molecules by the high-density plasma. The graded VS typically presents a threading dislocation density of about $5 \times 10^6 \mathrm{cm}^{-2}$[39]. The substrate temperature and plasma density was then reduced without interrupting the growth. The undoped $Si_{0.3}Ge_{0.7}/Ge/Si_{0.3}Ge_{0.7}$ QW stack was grown at 350 °C and a growth rate of about 0.5 nm^{-1} to limit Si intermixing and interface diffusion. A 2 nm Si cap was deposited after a short (60 s) interruption to facilitate the formation of the native oxide (the interruption reduces Ge contamination in the Si cap from residual precursor gases in the growth chamber). SIMS analysis indicates that boron levels are below the detection limit of 10^{15} cm^{-3} to a depth of at least 200 nm.

Device fabrication: The samples were processed in the IST Austria Nanofabrication Facility. A $6 \times 6\,\mathrm{mm}^2$ chip is cut out from a 4 inch wafer and cleaned before further processing. The Ohmic contacts are first patterned in a 100 keV electron beam lithography system, then a few nm of native oxide and the SiGe spacer is milled down by argon bombardment and subsequently a layer of 60 nm Pt is deposited in situ under an angle of 5°, to obtain reproducible contacts. No additional intentional annealing is performed. A mesa of 90 nm is etched in a reactive ion etching step. The native SiO_2 is removed by a 10 s dip in buffered HF before the gate oxide is deposited. The oxide is a 20 nm ALD aluminum oxide (Al_2O_3) grown at 300 °C, which unintentionally anneals the Ohmic contacts resulting in a low resistance contact to the carriers in the quantum well. The top gates are first patterned via ebeam lithography and then a Ti/Pd 3/27 nm layer is deposited in an electron beam evaporator. The thinnest gates are 30 nm wide and 30 nm apart. An additional thick gate metal layer is subsequently written and deposited and serves to overcome the Mesa step and allow wire bonding of the sample without shorting gates together. Quantum dots are formed by means of depletion gates (Fig. 1c). The lower gates (LB, L, CB, R, RB) form a double quantum dot (DQD) system and the upper gates tune a charge sensor (CS) dot. The separation gates in the middle are tuned to maximize the CS sensitivity to charge transitions in the DQD. An LC-circuit connected to a CS ohmic contact allows fast read-out through microwave reflectometry. LB and RB are further connected to fast gate lines enabling fast control of the energy levels in the DQD.

ACKNOWLEDGMENTS This research was supported by the Scientific Service Units of IST Austria through resources provided by the MIBA Machine Shop and the nanofabrication facility. This project has received funding from the European Union's Horizon 2020 research and innovation program under the Marie Sklodowska-Curie grant agreement No. 844511, No.

75441, and by the FWF-P 30207 project. A.B. acknowledges support from the EU Horizon-2020 FET project microSPIRE, ID: 766955. M.B. and J.A. acknowledge funding from Generalitat de Catalunya 2017 SGR 327. ICN2 is supported by the Severo Ochoa program from Spanish MINECO (Grant No. SEV-2017-0706) and is funded by the CERCA Programme / Generalitat de Catalunya. Part of the present work has been performed in the framework of Universitat Autònoma de Barcelona Materials Science PhD program. Part of the HAADF-STEM microscopy was conducted in the Laboratorio de Microscopias Avanzadas at Instituto de Nanociencia de Aragon-Universidad de Zaragoza. ICN2 acknowledge support from CSIC Research Platform on Quantum Technologies PTI-001. M.B. acknowledges funding from AGAUR Generalitat de Catalunya FI PhD grant.

DATA AVAILABILITY All data included in this work will be available from the IST Austria repository.

Author Contributions D.J. fabricated the sample, performed the experiments and data analysis. D.J., A.H and I.P. developed the fabrication recipe. D.J., A.H, O.S. and M. Bor. performed pre-characterizing measurements on equivalent samples. D.C. and A.B. designed the SiGe heterostructure. A.B. performed the growth supervised by G. I.. D.C. performed the x-ray diffraction measurements and simulations. G.T. performed Hall effect measurements, supervised by D.C.. P.M.M. derived the theoretical model. M.Bot. and J.A. performed the atomic resolution (S)TEM structural and EELS compositional related characterization and calculated the strain by using GPA. D.J., A.H., J.K, A.C., F.M., J.S.M and G.K. discussed the qubit data. D.J. and G.K. wrote the manuscript with input from all the authors. G.I. and G.K. initiated and supervised the project.

References

[1] Vandersypen, L. M. K. *et al.* Interfacing spin qubits in quantum dots and donors—hot, dense, and coherent. *npj Quantum Information* **3** (2017).

[2] Hendrickx, N. W. *et al.* A four-qubit germanium quantum processor. *arXiv: 2009.04268 [cond-mat]* (2020).

[3] Stehlik, J. *et al.* Fast charge sensing of a cavity-coupled double quantum dot using a josephson parametric amplifier. *Physical Review Applied* **4** (2015).

[4] Burkard, G., Gullans, M. J., Mi, X. & Petta, J. R. Superconductor–semiconductor hybrid-circuit quantum electrodynamics. *Nature Reviews Physics* **2**, 129–140 (2020).

[5] Leonard, E. *et al.* Digital coherent control of a superconducting qubit. *Physical Review Applied* **11** (2019).

[6] Schupp, F. J. *et al.* Sensitive radiofrequency readout of quantum dots using an ultra-low-noise SQUID amplifier. *Journal of Applied Physics* **127**, 244503 (2020).

[7] Wallraff, A. *et al.* Strong coupling of a single photon to a superconducting qubit using circuit quantum electrodynamics. *Nature* **431**, 162–167 (2004).

[8] Levy, J. Universal quantum computation with spin-1/2pairs and heisenberg exchange. *Physical Review Letters* **89** (2002).

[9] Petta, J. R. Coherent manipulation of coupled electron spins in semiconductor quantum dots. *Science* **309**, 2180–2184 (2005).

[10] Hendrickx, N. W. *et al.* Gate-controlled quantum dots and superconductivity in planar germanium. *Nature Communications* **9** (2018).

[11] Vigneau, F. *et al.* Germanium quantum-well Josephson field-effect transistors and interferometers. *Nano Letters* **19**, 1023–1027 (2019).

[12] Amitonov, S. V., Spruijtenburg, P. C., Vervoort, M. W. S., van der Wiel, W. G. & Zwanenburg, F. A. Depletion-mode quantum dots in intrinsic silicon. *Applied Physics Letters* **112**, 023102 (2018).

[13] Scappucci, G. *et al.* The germanium quantum information route. *arXiv: 2004.08133 [cond-mat], Nature Review Materials (accepted)* (2020).

[14] Kloeffel, C., Trif, M. & Loss, D. Strong spin-orbit interaction and helical hole states in Ge/Si nanowires. *Physical Review B* **84** (2011).

[15] Froning, F. N. M. *et al.* Ultrafast hole spin qubit with gate-tunable spin-orbit switch. *arXiv: 2006.11175 [cond-mat]* (2020).

[16] Wang, K. *et al.* Ultrafast operations of a hole spin qubit in ge quantum dot. *arXiv: 2006.12340 [cond-mat]* (2020).

[17] Lodari, M. *et al.* Light effective hole mass in undoped Ge/SiGe quantum wells. *Physical Review B* **100** (2019).

[18] Loss, D. & DiVincenzo, D. P. Quantum computation with quantum dots. *Physical Review A* **57**, 120–126 (1998).

[19] Watzinger, H. *et al.* A germanium hole spin qubit. *Nature Communications* **9** (2018).

[20] Hendrickx, N. W., Franke, D. P., Sammak, A., Scappucci, G. & Veldhorst, M. Fast two-qubit logic with holes in germanium. *Nature* **577**, 487–491 (2020).

[21] Katsaros, G. *et al.* Observation of spin-selective tunneling in SiGe nanocrystals. *Physical Review Letters* **107** (2011).

[22] Petta, J. R., Lu, H. & Gossard, A. C. A coherent beam splitter for electronic spin states. *Science* **327**, 669–672 (2010).

[23] Ares, N. *et al.* Nature of tunable HolegFactors in quantum dots. *Physical Review Letters* **110** (2013).

[24] Studenikin, S. A. *et al.* Enhanced charge detection of spin qubit readout via an intermediate state. *Applied Physics Letters* **101**, 233101 (2012).

[25] Orona, L. A. *et al.* Readout of singlet-triplet qubits at large magnetic field gradients. *Physical Review B* **98** (2018).

[26] Wu, X. *et al.* Two-axis control of a singlet-triplet qubit with an integrated micromagnet. *Proceedings of the National Academy of Sciences* **111**, 11938–11942 (2014).

[27] Hofmann, A. *et al.* Assessing the potential of Ge/SiGe quantum dots as hosts for singlet-triplet qubits. *arXiv: 1910.05841 [cond-mat]* (2019).

[28] Dial, O. E. *et al.* Charge noise spectroscopy using coherent exchange oscillations in a singlet-triplet qubit. *Physical Review Letters* **110** (2013).

[29] Takeda, K., Noiri, A., Yoneda, J., Nakajima, T. & Tarucha, S. Resonantly driven singlet-triplet spin qubit in silicon. *Physical Review Letters* **124** (2020).

[30] Wang, X. *et al.* Composite pulses for robust universal control of singlet–triplet qubits. *Nature Communications* **3** (2012).

[31] Medford, J. *et al.* Scaling of dynamical decoupling for spin qubits. *Physical Review Letters* **108** (2012).

[32] Martins, F. *et al.* Noise suppression using symmetric exchange gates in spin qubits. *Physical Review Letters* **116** (2016).

[33] Bluhm, H. *et al.* Dephasing time of GaAs electron-spin qubits coupled to a nuclear bath exceeding 200 s. *Nature Physics* **7**, 109–113 (2010).

[34] Maune, B. M. *et al.* Coherent singlet-triplet oscillations in a silicon-based double quantum dot. *Nature* **481**, 344–347 (2012).

[35] Maurand, R. *et al.* A CMOS silicon spin qubit. *Nature Communications* **7** (2016).

[36] Reed, M. *et al.* Reduced sensitivity to charge noise in semiconductor spin qubits via symmetric operation. *Physical Review Letters* **116** (2016).

[37] Nichol, J. M. *et al.* High-fidelity entangling gate for double-quantum-dot spin qubits. *npj Quantum Information* **3** (2017).

[38] Rössner, B., Chrastina, D., Isella, G. & von Känel, H. Scattering mechanisms in high-mobility strained Ge channels. *Applied Physics Letters* **84**, 3058–3060 (2004).

[39] Marchionna, S., Virtuani, A., Acciarri, M., Isella, G. & von Kaenel, H. Defect imaging of SiGe strain relaxed buffers grown by LEPECVD. *Materials Science in Semiconductor Processing* **9**, 802–805 (2006).